

# Fe<sub>3</sub>O<sub>4</sub>-Functionalized Boron Nitride Nanosheets as Novel Adsorbents for Removal of Arsenic(III) from Contaminated Water

Raghubeer S. Bangari, Vivek K. Yadav, Jayant K. Singh,\* and Niraj Sinha\*



Cite This: *ACS Omega* 2020, 5, 10301–10314



Read Online

ACCESS |



Metrics & More

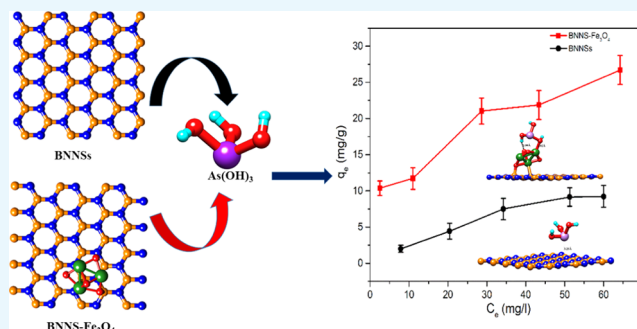


Article Recommendations



Supporting Information

**ABSTRACT:** We report the application of Fe<sub>3</sub>O<sub>4</sub>-functionalized boron nitride nanosheets (BNNS-Fe<sub>3</sub>O<sub>4</sub> nanocomposite) for the remediation of As(III) ions from contaminated water. The specific surface area of the nanocomposite has been found as 179.5 m<sup>2</sup> g<sup>-1</sup>. Due to its superparamagnetic nature at room temperature, the nanocomposite can be easily isolated from the solution under an external magnetic field. For As(III) ions, the maximum adsorption capacity of the nanocomposite is obtained as 30.3 mg g<sup>-1</sup>, which is approximately 4 times more than that of the bare BNNSs (8.5 mg g<sup>-1</sup>). The results from density functional theory calculations are also in close agreement with experimental findings and show that As(OH)<sub>3</sub> binds more (~4 times) efficiently to the BNNS-Fe<sub>3</sub>O<sub>4</sub> nanocomposite than the bare BNNSs, implying a 4 times higher adsorption capacity of the nanocomposite. Especially, it is found that the synthesized nanocomposite could lessen the concentration of As(III) ions from 134 to 2.67 ppb in a solution at 25 °C. On increasing the temperature to 35 °C, the level of As(III) ions could be reduced from 556 to 10.29 ppb, which is close to the limit prescribed by the World Health Organization. The adsorbent was easily separable and showed regeneration properties. These outcomes depict the prospect of using BNNS-Fe<sub>3</sub>O<sub>4</sub> nanocomposites as commercial adsorbents for the removal of As(III) ions from contaminated water.



## 1. INTRODUCTION

The contamination of natural water by arsenic (As) has become a global problem. According to estimates, 70.4 million people in India and 140 million people around the globe are exposed to drink As-contaminated groundwater.<sup>1,2</sup> Exposure to As-contaminated water in the long term may result in cancer, neurological diseases, and muscular weakness, to name a few. Due to its extreme toxicity, the World Health Organization (WHO) has set the As standard for drinking water at 10 ppb.<sup>3–6</sup> As a result, many water sources have become unsafe. To avoid the potential hazards to human health and the environment in general, it is necessary to remove excess As from drinking water. Arsenic is found mainly as arsenite [As(III)] and arsenate [As(V)] forms in natural water. As(III) is 60 times more toxic than As(V) and exists mainly in groundwater. Also, it has been reported that toxicity of inorganic As compounds is approximately 100 times greater than that of organic As compounds.<sup>7</sup> Several technologies such as ion exchange, oxidation, coagulation or flocculation, membrane filtration, reverse osmosis, and adsorption have been proposed for the remediation of As.<sup>8,9</sup> Among them, adsorption has been widely used due to its simplicity of design, ease of operation, low cost, ease of regeneration, and sludge-free operation.

Against this backdrop, different kinds of materials have been synthesized and are being used for the removal of As from

contaminated water. The traditional materials that are being used include fly ash, coal-based carbon, activated carbon, metal oxides, goethite, and chitosan resin, to name a few.<sup>10</sup> Due to their unique characteristics including a large surface-to-volume ratio, nanomaterials have proven to be excellent candidates for the adsorption of both As(III) and As(V) from contaminated water.<sup>11–14</sup> Among them, the adsorbents based on iron oxides such as magnetite (Fe<sub>3</sub>O<sub>4</sub>), hematite (α-Fe<sub>2</sub>O<sub>3</sub>), and magnetic maghemite (γ-Fe<sub>2</sub>O<sub>3</sub>) have drawn tremendous attention owing to the low cost of raw materials, easy preparation, nontoxic nature, hydrophilicity, ease of separation, and superior performance for As-ion adsorption.<sup>15,16</sup> However, the small particle size and instability of iron oxide nanomaterials make their application difficult in continuous-flow systems.<sup>17</sup> To overcome this limitation and enhance their adsorption performance further, other nanomaterials have been used to incorporate magnetic oxides on their surface in the form of substrates that included nanotubes and nanosheets.<sup>18–24</sup> In

Received: December 15, 2019

Accepted: April 12, 2020

Published: April 29, 2020



one of the seminal papers, Chandra et al. removed As(III) by the incorporation of magnetite on the surface of reduced graphene oxide. The adsorption capacity was found to be 13.1 mg g<sup>-1</sup>.<sup>18</sup> Further, Andjelkovic et al. reduced 150 ppb of As(III) of real water sample to 10 ppb (i.e., 93.3% removal) with the three-dimensional (3D) graphene–iron oxide nanoparticle aerogel composite and an adsorption capacity of 13.42 mg g<sup>-1</sup>.<sup>22</sup> Carbon nanotubes (CNTs) have also been coated with iron oxide for As(III) remediation.<sup>19,20</sup> The iron oxide–multiwalled carbon nanotube (Fe–MWCNT) hybrid synthesized by Ntim and Mitra, with an adsorption capacity of 1723 μg g<sup>-1</sup>, worked effectively to bring down the arsenic level to the drinking water level.<sup>19</sup> Using the magnetic iron oxide/CNT combination, Ma et al. demonstrated the adsorption capacity of As(III) as 8.13 mg g<sup>-1</sup>.<sup>20</sup> Iron and aluminum oxide-coated 3D-organized mesoporous silica has also been reported in the literature for the removal of As(III) from synthetic contaminated water.<sup>21</sup> However, the adsorption capacity was found to be low (0.21 mg g<sup>-1</sup>).

An adsorbent to be used for water remediation should have a high adsorption capacity in addition to a good physical and chemical stability, large surface area, nontoxicity, high recyclability, and ease of separation. In light of these requirements, we have synthesized and characterized boron nitride nanosheets (BNNSs) of large specific surface area. The unique bipolar nature and planar bonding make BNNSs chemically stable. BNNSs have been functionalized with Fe<sub>3</sub>O<sub>4</sub> nanoparticles, and the adsorption performance studies of As(III) of both unmodified and Fe<sub>3</sub>O<sub>4</sub> functionalized BNNSs have been carried out. In addition to enhancing the adsorption capacity, the Fe<sub>3</sub>O<sub>4</sub>-functionalized nanocomposite adsorbent easily separates from water under a magnetic field. Further, the experimentally calculated adsorption capacities are in agreement with the density functional theory (DFT) simulations. The results demonstrate the potential of these nanocomposites for arsenic removal from water.

## 2. MATERIALS AND METHODS

**2.1. Computational Details: DFT Calculations.** The initial structure of the boron nitride sheet was prepared using visual molecular dynamics (VMD),<sup>25</sup> whereas other structures such as Fe<sub>3</sub>O<sub>4</sub> and As(OH)<sub>3</sub> were built and optimized using Avogadro.<sup>26</sup> Theoretical calculations were performed using first-principles DFT, as implemented in the Quantum ESPRESSO<sup>27</sup> code. Generalized gradient approximation (GGA) with the Perdew–Burke–Ernzerhof (PBE)<sup>28</sup> exchange–correlation functional of ultrasoft pseudopotentials type was used in this case. Ultrasoft pseudopotentials were generated using the Rappe–Rabe–Kaxiras–Joannopoulos (RRKJ3) method.<sup>29</sup> The Kohn–Sham wave functions were expanded in a plane-wave basis set with kinetic energy cutoffs of 65 and 600 Ry for charge density. Brillouin zone (BZ) integration with a Monkhorst–Pack<sup>30</sup> *k*-point grid of 5 × 5 × 1 was used for geometry optimization, and 10 × 10 × 1 for self-consistent calculations. The cell parameters and atomic positions were relaxed until the forces on each ion and atom became smaller than 0.03 eV Å<sup>-1</sup>. To avoid interaction within periodic images, 20 Å of vacuum was used between periodically repeated layers. As is well known that the van der Waals (vdW) interaction is important for adsorption energy calculation, we applied Grimme's dispersion correction to DFT calculations (DFTD3)<sup>31</sup> for the PBE functional. In the current work, the binding energy (BE) calculations of

As(OH)<sub>3</sub> on both the adsorbents have been computed and compared. The BEs were calculated using the following relations

$$\begin{aligned} \text{BE} &= E(\text{BNNS} - \text{Fe}_3\text{O}_4 + \text{As}(\text{OH})_3) \\ &\quad - [E(\text{BNNS} - \text{Fe}_3\text{O}_4) + E(\text{As}(\text{OH})_3)], \\ &\quad (\text{BNNS} - \text{Fe}_3\text{O}_4) \end{aligned}$$

$$\begin{aligned} \text{BE} &= E(\text{BNNSs} + \text{As}(\text{OH})_3) \\ &\quad - [E(\text{BNNSs}) + E(\text{As}(\text{OH})_3)]. \quad (\text{BNNSs}) \end{aligned}$$

**2.2. Experiments. 2.2.1. Materials.** The chemicals used in this study were the same as the ones reported in our earlier work<sup>32</sup> and are mentioned in the [Supporting Information](#). In addition, hydrochloric acid (~37%) and methanol were received from Thermo Fisher Scientific, India. Sodium arsenite (≥98.5% purity) that was used as a source of As(III) and the standard As ion solution were purchased from Loba Chemie, India.

**2.2.2. Synthesis of BNNSs.** BNNSs were synthesized by easily available and low-cost precursors boric acid and urea. The molar ratio used was 1:30. Accurately weighted (using ME 204, Mettler Toledo electronic weighing machine) boric acid and urea were mixed physically with a mortar and pestle. Further, methanol and deionized (DI) water were added into the mixture and subsequently dried inside an oven at 45 °C. Afterward, the dried mixture was placed in a quartz boat and kept in a tubular furnace. The mixture was heated up to 900 °C and maintained at this temperature in a N<sub>2</sub> gas environment for 2 h.<sup>33</sup> Once the chemical reaction was complete, the temperature of the furnace was decreased gradually to room temperature. At the end, white BNNSs were received.

**2.2.3. Synthesis of BNNS-Fe<sub>3</sub>O<sub>4</sub> Nanocomposites.** To functionalize BNNSs with Fe<sub>3</sub>O<sub>4</sub> nanoparticles, a known amount of BNNSs was added in 100 mL of DI water. Thereafter, the solution was subjected to ultrasonication (Oscar, India) for 1 h. To synthesize Fe<sub>3</sub>O<sub>4</sub> nanoparticles, FeCl<sub>3</sub>·6H<sub>2</sub>O and FeCl<sub>2</sub>·4H<sub>2</sub>O in a molar ratio of 2:1 were added to the stirring solution. During the start of the reaction, the pH of the solution was adjusted to 8.0 by a dropwise addition of 3 mL of NH<sub>4</sub>OH through a syringe.<sup>34</sup> The solution was magnetically stirred further for 3.5 h. The whole reaction was performed under a N<sub>2</sub> gas environment. At the end of the reaction, the synthesized product was washed with ultrapure deionized (DI) water and dried at 65 °C to get Fe<sub>3</sub>O<sub>4</sub>-coated BNNSs.

**2.2.4. Characterization and Measurements.** Imaging techniques such as field emission scanning electron microscopy (FESEM, Carl Zeiss) and high-resolution transmission electron microscopy (HRTEM, FEI Titan G2 60-300 microscope) were used to characterize the morphologies, elemental distribution, and nature (amorphous/crystalline) of synthesized materials. A N<sub>2</sub> gas adsorption–desorption isotherm at -196 °C (Quantachrome Autosorb iQ) was used to calculate the specific surface area (SBET), pore size distribution, and pore volume. To examine the structure of BNNSs and BNNS-Fe<sub>3</sub>O<sub>4</sub>, X-ray diffraction (XRD, Panalytical X'Pert Powder) was used. The plots of the synthesized products were noted by Cu Kα radiation (λ = 1.506 Å) from 10 to 70°. The surface functional groups were analyzed by Fourier transform infrared (FTIR) spectroscopy (PerkinElmer Spectrum Two spectrometer). The saturation magnetization (M<sub>s</sub>) of the nano-

composite was determined by a vibrating sample magnetometer (VSM, EV7 ADE-DMS) at room temperature. The concentrations of As(III) in the aqueous solution were measured by inductively coupled plasma mass spectroscopy (Agilent 7900, ICP-MS) with the help of a standard calibration curve prepared by the standard solution of As. The synthesized adsorbent was mounted on conductive carbon tape and examined by X-ray photoelectron spectroscopy (XPS, PHI 5000 VersaProbe-ULVAC-PHI Inc.). Raman spectroscopy was carried out using a 532 nm laser (Airix micro-Raman spectrometer) to characterize the adsorbed sample.

**2.2.5. Arsenic(III) Adsorption Experiments.** All of the adsorption experiments were performed at room temperature (25 °C). The batch experiments were performed to determine the effect of various adsorption parameters (initial pH, contact time, dosage, and isotherm) on the As(III) adsorption capacity of both the adsorbents. In the batch experiments, 0.4 g per liter of adsorbents were added into As(III) (25 mL, 25 mg L<sup>-1</sup>). Subsequently, the solutions were subjected to ultrasonication for 5 min to disperse the adsorbents into the As(III) solution. The initial pH, kinetics, and dosage studies were performed by fixing the concentration of As(III) solution at 25 mg L<sup>-1</sup>. The effect of pH on the adsorption capacity was studied by varying the pH in the range of 2–12. HCl (0.1 M) and NaOH (0.1 M) solutions were used to maintain the initial pH. All of the adsorption experiments were conducted at 200 rpm and 25 °C inside a thermally controlled orbital shaker purchased from Mahendra Scientific, India. After taking out the equilibrated samples, a 0.22 μm syringe filter (Millex) was used to separate the adsorbents. It was followed by the determination of As(III) concentration in the aqueous solution using ICP-MS. The following equation was used to calculate the equilibrium uptake ( $q_e$  in mg g<sup>-1</sup>)

$$q_e = \frac{(C_0 - C_e)V}{m} \quad (1)$$

where  $C_0$  (mg l<sup>-1</sup>) is the initial As(III) ion concentration,  $C_e$  (mg l<sup>-1</sup>) is the equilibrium As(III) ion concentration,  $V$  (l) is the volume of solution, and  $m$  (g) is the mass of the adsorbent. In this work, all of the experiments were performed in triplicate and their mean values have been presented.

**2.2.5.1. Kinetic Studies.** The kinetic studies were performed by adding a known amount of adsorbent into 100 mL of the As(III) solution (25 mg l<sup>-1</sup>) at the optimum pH value obtained through the pH study. Thereafter, the experimental data were analyzed with pseudo-first-order (PFO) and pseudo-second-order (PSO) kinetic models. These models are used to determine the kinetic parameters of BNNSs and BNNS-Fe<sub>3</sub>O<sub>4</sub>. The linear forms of PFO and PSO models are expressed using eqs 2 and 3, respectively, as

$$\ln(q_e - q_t) = \ln q_e - k_1 t \quad (2)$$

$$\frac{t}{q_t} = \frac{1}{k_2 q_e^2} + \frac{1}{q_e} \quad (3)$$

where  $q_t$  is the amount of adsorbed solute at time  $t$ ,  $k_1$  (min<sup>-1</sup>) is the pseudo-first-order rate constant, and  $k_2$  (g mg<sup>-1</sup>min<sup>-1</sup>) is the pseudo-second-order kinetic rate constant.

**2.2.5.2. Adsorption Isotherm Study.** This study was carried out to investigate the effect of the initial concentration of As(III) on the adsorption capacity. The dose was kept constant at 0.4 g l<sup>-1</sup>, and the pH was maintained at the value obtained

through the optimization study. Thereafter, samples were transferred to a thermo-controlled orbital shaker. It was kept at 25 °C and 200 rpm. Moreover, two isotherm models, viz., Langmuir and Freundlich, were applied to analyze the adsorption data. The Langmuir isotherm is represented by the following equation

$$q_e = \frac{q_m C_e K_L}{1 + C_e K_L} \quad (4)$$

In eq 4,  $K_L$  (mL mg<sup>-1</sup>) and  $q_m$  (mg g<sup>-1</sup>) denote the Langmuir adsorption equilibrium constant and the maximum adsorption capacity of the adsorbent, respectively. Similarly, the following equation is used to represent the Freundlich isotherm

$$q_e = K_F C_e^{1/n} \quad (5)$$

In eq 5,  $K_F$  is a constant that measures the adsorption capacity, while  $n$  is another constant that measures the adsorption intensity.<sup>35</sup>

### 3. RESULTS AND DISCUSSION

**3.1. DFT Calculations on As(III) Adsorption.** To assess the binding ability of As with Fe<sub>3</sub>O<sub>4</sub>, the first-principles DFT approach was used to compute the interaction strength between As(OH)<sub>3</sub> with both the adsorbents. The theoretically optimized (relaxed) structures of BNNSs and As(OH)<sub>3</sub> are displayed in Figure 1a,b, respectively. Similarly, the side and top views of the BNNS-Fe<sub>3</sub>O<sub>4</sub> nanocomposite are displayed in Figure 1c,d, respectively, from which one can see the formation of the BNNS-Fe<sub>3</sub>O<sub>4</sub> nanocomposite through B–O and N–Fe bonds. The computed average distance between the BNNSs and the Fe<sub>3</sub>O<sub>4</sub> surface was found to be ~2.45 Å. Further, the geometric relaxation of As(OH)<sub>3</sub> with BNNSs and BNNS-Fe<sub>3</sub>O<sub>4</sub>-As(OH)<sub>3</sub> structures were performed using a similar approach stated above, and the BEs were evaluated later using the same method described in Section 2.1. The computationally relaxed structures of BNNS-As(OH)<sub>3</sub> and BNNS-Fe<sub>3</sub>O<sub>4</sub>-As(OH)<sub>3</sub> systems are shown in Figure 2a,b, which were computed using the DFT approach. The calculated values of BEs for both As(OH)<sub>3</sub> with BNNSs and BNNS-Fe<sub>3</sub>O<sub>4</sub> nanocomposite were -27.160 and -113.272, in units of kJ mol<sup>-1</sup>, respectively. These results demonstrate that As(OH)<sub>3</sub> shows ~4.15 times more binding energy strength with BNNS-Fe<sub>3</sub>O<sub>4</sub> than the unmodified BNNSs. This indicates a higher adsorption capacity for BNNS-Fe<sub>3</sub>O<sub>4</sub> between the two adsorbents.

**3.2. Characterization of the Adsorbents.** The morphology, crystallinity, and elemental distribution of the synthesized adsorbents were characterized by FESEM and HRTEM. The layered structure of the sheets can be easily seen by FESEM (see Figures S1a). In the HRTEM image in Figure 3, the fringes of BNNSs are clearly seen in Figure 3a-i. Moreover, the BNNS-Fe<sub>3</sub>O<sub>4</sub> nanocomposite depicts the cubic structure of the Fe<sub>3</sub>O<sub>4</sub> nanoparticles (see Figure 3b-i) deposited on the layers of BNNSs. The selected area electron diffraction (SAED) pattern of BNNSs shows the diffuse rings, implying its amorphous nature. Each ring corresponds to the (002), (100), and (101) planes as we move in the outward direction from the center of the ring, as shown in Figure 3c. On the other hand, the SAED pattern of the BNNS-Fe<sub>3</sub>O<sub>4</sub> nanocomposite shows rings with spots as shown in Figure 3d. This indicates the crystalline nature of the nanocomposite. The high-angle annular dark film (HAADF) image and elemental

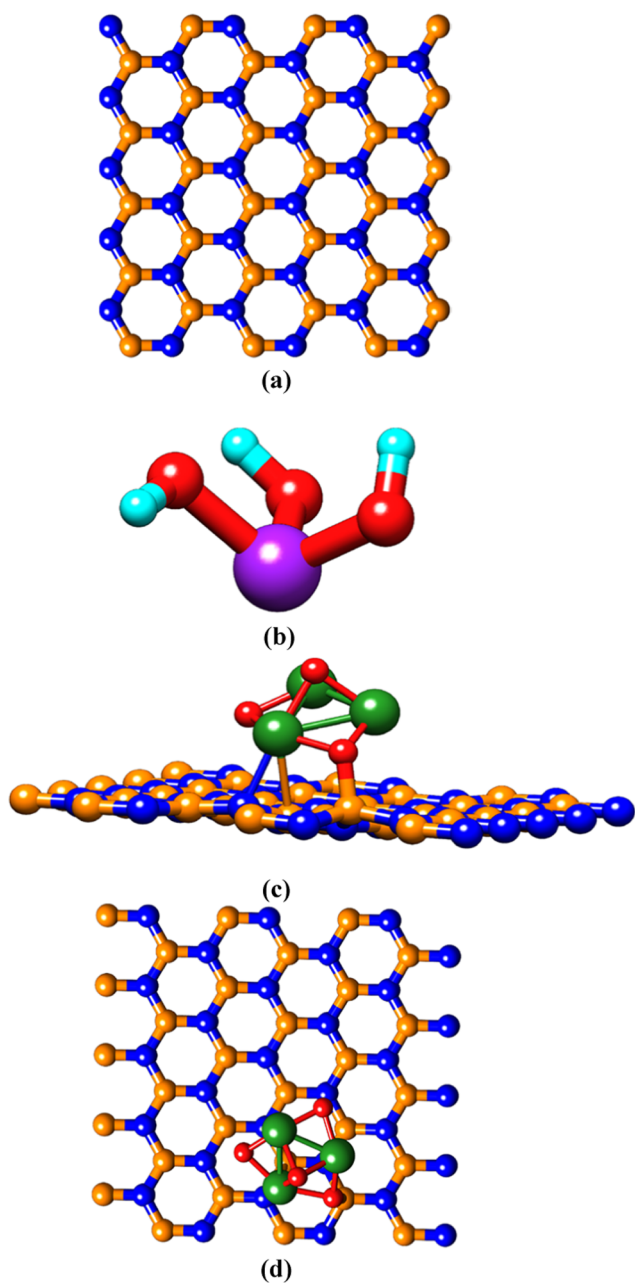


**Figure 1.** Optimized geometries of (a) BNNSs, (b) As(OH)<sub>3</sub>, (c) BNNS-Fe<sub>3</sub>O<sub>4</sub> structure (side view), and (d) BNNS-Fe<sub>3</sub>O<sub>4</sub> structure (top view). The atoms colors are B (orange), N (blue), Fe (green), H (cyan), As (purple), and O (red).

mapping (see Figure 3e,f) show the uniform distribution of BNNSs and Fe<sub>3</sub>O<sub>4</sub> nanoparticles as well as boron and nitrogen on BNNS-Fe<sub>3</sub>O<sub>4</sub> nanocomposite, respectively. The nitrogen (N<sub>2</sub>) adsorption–desorption isotherms (see Figure S2) of both the adsorbents were used to calculate the specific surface area (SBET) and pore size distribution (PSD). The SBET values for BNNSs and BNNS-Fe<sub>3</sub>O<sub>4</sub> were obtained as 1801.9 and 179.5 m<sup>2</sup> g<sup>-1</sup>, respectively. The reduction in the total pore volume and the corresponding specific surface area of the BNNS-Fe<sub>3</sub>O<sub>4</sub> nanocomposite may be attributed to the filling of pores of BNNSs during the growth of magnetic (Fe<sub>3</sub>O<sub>4</sub>) nanoparticles on its surface. A decrease in the specific surface area with magnetite loading was also observed in the case of graphene oxide.<sup>18</sup> The XRD patterns of BNNSs and BNNSs-

Fe<sub>3</sub>O<sub>4</sub> are shown in Figure 4. BNNSs show their characteristic diffraction peaks at 25.4 and 41.2° that correspond to (002) and (101) planes. Due to the broadening of diffraction peaks, two close peaks (100) and (101) were merged at 41.2°. The peak broadening of BNNSs indicates the amorphous behavior of BNNSs. The XRD pattern of BNNS-Fe<sub>3</sub>O<sub>4</sub> shows various crystalline peaks at  $2\theta = 30.37, 35.65, 43.53, 53.85, 57.37,$  and  $63.07^\circ$ .<sup>36–38</sup> These peaks correspond to the (220), (311), (400), (422), (511), and (440) planes. The positions of all of the peaks and the corresponding planes matched with JCPDS card no. 19-0629. Further, all of the planes perfectly match and are well supported by the corresponding SAED patterns.

To characterize further, FTIR spectroscopy was used to record the vibrating signature of the functional groups that existed on the synthesized materials through transmission/adsorption spectra in the range of 4000–400 cm<sup>-1</sup>. Figure 5 shows the FTIR spectra of BNNSs and BNNS-Fe<sub>3</sub>O<sub>4</sub> with black and red colors, respectively. The spectra of BNNSs show two characteristics peaks at 780 and 1380 cm<sup>-1</sup>. The peak at 780 cm<sup>-1</sup> corresponds to the out-of-plane vibration of B–N–B, while the peak at 1380 cm<sup>-1</sup> represents the in-plane vibration of B–N–B. The peak at ~1644 cm<sup>-1</sup> corresponds to the bending vibration of H–O–H from the water molecule. The low-intensity peaks at 2852 and 2925 cm<sup>-1</sup> represent the –NH<sub>2</sub> group formation at the edges.<sup>39</sup> Finally, a broad peak is observed at 3415 cm<sup>-1</sup> that can be ascribed to the B–OH group.<sup>40</sup> In the case of BNNS-Fe<sub>3</sub>O<sub>4</sub>, the FTIR spectrum clearly shows the symmetric vibration of Fe–O at 583 cm<sup>-1</sup>. The out-of-plane vibration of B–N–B bonds and its intensity are related to the stacking order of BNNSs. The in-plane vibration of BNNSs at 1380 cm<sup>-1</sup> indicates no change in the structure of BNNSs after the formation of BNNS-Fe<sub>3</sub>O<sub>4</sub> nanocomposite. Moreover, the peak at 923 cm<sup>-1</sup> is due to the stretching vibration signals of Fe–O–Fe.

To determine the percentage composition of BNNS-Fe<sub>3</sub>O<sub>4</sub>, an XPS study was carried out. As can be seen in Figure 6, the percentages of boron, carbon, nitrogen, oxygen, and iron were found to be 12.2, 17.1, 6.4, 53.9, and 10.3, respectively. The high percentage of carbon was due to the black tape used to hold the sample during the XPS analysis. To separate BNNS-Fe<sub>3</sub>O<sub>4</sub> from water with the help of a magnet, a threshold value of Ms of the nanocomposite is needed to separate the BNNS-Fe<sub>3</sub>O<sub>4</sub> from water with the help of a magnet. The minimum value of Ms needed for separation is 18 emu g<sup>-1</sup>.<sup>41</sup> In the case of BNNS-Fe<sub>3</sub>O<sub>4</sub>, the Ms was determined as 47.39 emu g<sup>-1</sup> and is shown in Figure 7. The inset image shows the separated adsorbent from the aqueous solution. Therefore, one can easily separate the adsorbent (BNNS-Fe<sub>3</sub>O<sub>4</sub>) from the aqueous solution with the help of a magnet.

**3.3. Effects of Adsorption Parameters. 3.3.1. Effect of pH.** The surface charge of the adsorbent plays a decisive role in the adsorption process, which is directly affected by the pH of the solution among others. To investigate the surface charge,  $\zeta$ -potential measurements were performed to determine the point of zero charge (PZC). Additionally, the pH drift method was also used to find the same.<sup>42</sup> Both the methods confirmed the PZC of BNNSs and BNNS-Fe<sub>3</sub>O<sub>4</sub> at pH 2.88 and 2.1, respectively (see Figure 8a). The surface of BNNS-Fe<sub>3</sub>O<sub>4</sub> becomes positively and negatively charged if the pH value of the solution is below and above the PZC, respectively. The As(III) species depicts the neutral charge up to pH 8 due to the presence of H<sub>3</sub>AsO<sub>3</sub> species in the solution. The adsorption capacity increases with the increase in pH from 2

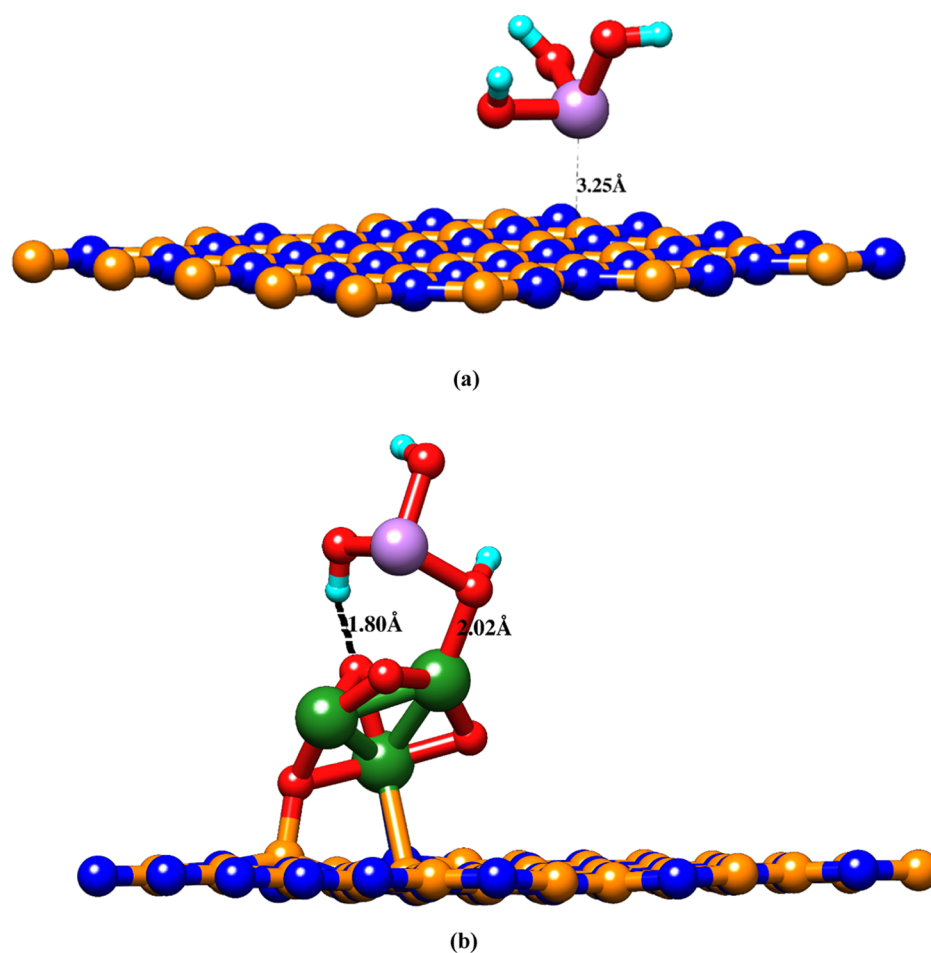


**Figure 2.** Structures obtained from DFT optimization: (a) BNNSs-As (OH)<sub>3</sub> and (b) BNNS-Fe<sub>3</sub>O<sub>4</sub>-As (OH)<sub>3</sub> nanocomposites. The atoms colors are B (orange), N (blue), Fe (green), H (cyan), As (purple), and O (red).

to 8 since there is no electrostatic attraction between the neutral H<sub>3</sub>AsO<sub>3</sub> and the positive surface of the adsorbents (see Figure 8b). Therefore, the increase of the adsorption capacity in the slightly alkaline solution can be attributed to the surface complexation reaction between the adsorbent surface and H<sub>3</sub>AsO<sub>3</sub>.<sup>43,44</sup> With a further increase in pH, As(III) becomes negatively charged due to the formation of H<sub>2</sub>AsO<sub>3</sub><sup>-1</sup> and HAsO<sub>3</sub><sup>-2</sup> species.<sup>45</sup> Therefore, the adsorption capacity decreases rapidly due to the electrostatic repulsion between the arsenic species and negatively charged adsorbent. Another reason behind the decline in the adsorption capacity of both the adsorbents with an increase in the pH value beyond 8 may be the competition between H<sub>2</sub>AsO<sub>3</sub><sup>-</sup> (the form in which As(III) exists) and the high OH<sup>-</sup> concentration present in the aqueous solution for active sites of the adsorbents.<sup>46</sup>

**3.3.2. Effect of Adsorbent Dose.** To investigate the effect of adsorbent dose on the adsorption capacity, the dose was increased from 0.2 to 0.8 g l<sup>-1</sup>. As seen in Figure 9, the percentage removal of As(III) in the case of BNNS-Fe<sub>3</sub>O<sub>4</sub> increases from 22 to 71% with an increase in the amount of adsorbent. The corresponding adsorption capacity decreases from 25.38 to 20.43 mg g<sup>-1</sup> (see Figure 9a). The adsorption behavior shown by BNNS-Fe<sub>3</sub>O<sub>4</sub> is quite common. The higher amount of adsorbent decreases the number of available active sites due to aggregation. Consequently, the adsorption capacity decreases. On the other hand, the behavior is quite different in the case of BNNSs. With an increase in the dose from 0.2 to

0.4 g l<sup>-1</sup>, the percentage removal increases from 7.4 to 12% and the corresponding adsorption capacity decreases from 8.25 to 7.25 mg g<sup>-1</sup>. A further increase in the dose from 0.4 to 0.8 g l<sup>-1</sup> results in a decrease in both the percentage removal (from 12 to 5.64%) and the adsorption capacity (from 7.25 to 1.62 mg g<sup>-1</sup>) (see Figure 9b). This behavior can be explained as follows. The percentage removal depends on the number of available active sites. As the amount of adsorbent increases, the strong van der Waals force between the BN layers increases. It leads to the aggregation of two-dimensional (2D) layers of boron nitride. Consequently, there is a decrease in the number of available active sites for adsorption.<sup>47,48</sup> Therefore, the adsorption capacity decreases.

**3.3.3. Adsorption Kinetics.** To carry out the contact time study, the adsorbent dose was taken as 0.4 g l<sup>-1</sup>. The adsorption capacities of both the adsorbents increase with time, as shown in Figure 10. The adsorption capacity of BNNS-Fe<sub>3</sub>O<sub>4</sub> increases rapidly up to 120 min. Thereafter, the adsorption increases gradually and achieves equilibrium at 480 min. The adsorption capacity value starts from 10.0 mg g<sup>-1</sup> and attains equilibrium at 24.5 mg g<sup>-1</sup>. The adsorption of As(III) for BNNSs gently increases with time instead. The adsorption plot becomes a plateau after 240 min. The kinetic behavior shown by both the adsorbents is quite different. This is mainly due to the high affinity of the BNNS-Fe<sub>3</sub>O<sub>4</sub> nanocomposite for As(III) due to the presence of Fe<sub>3</sub>O<sub>4</sub>. Therefore, the adsorption rate is initially high. It saturates later due to the

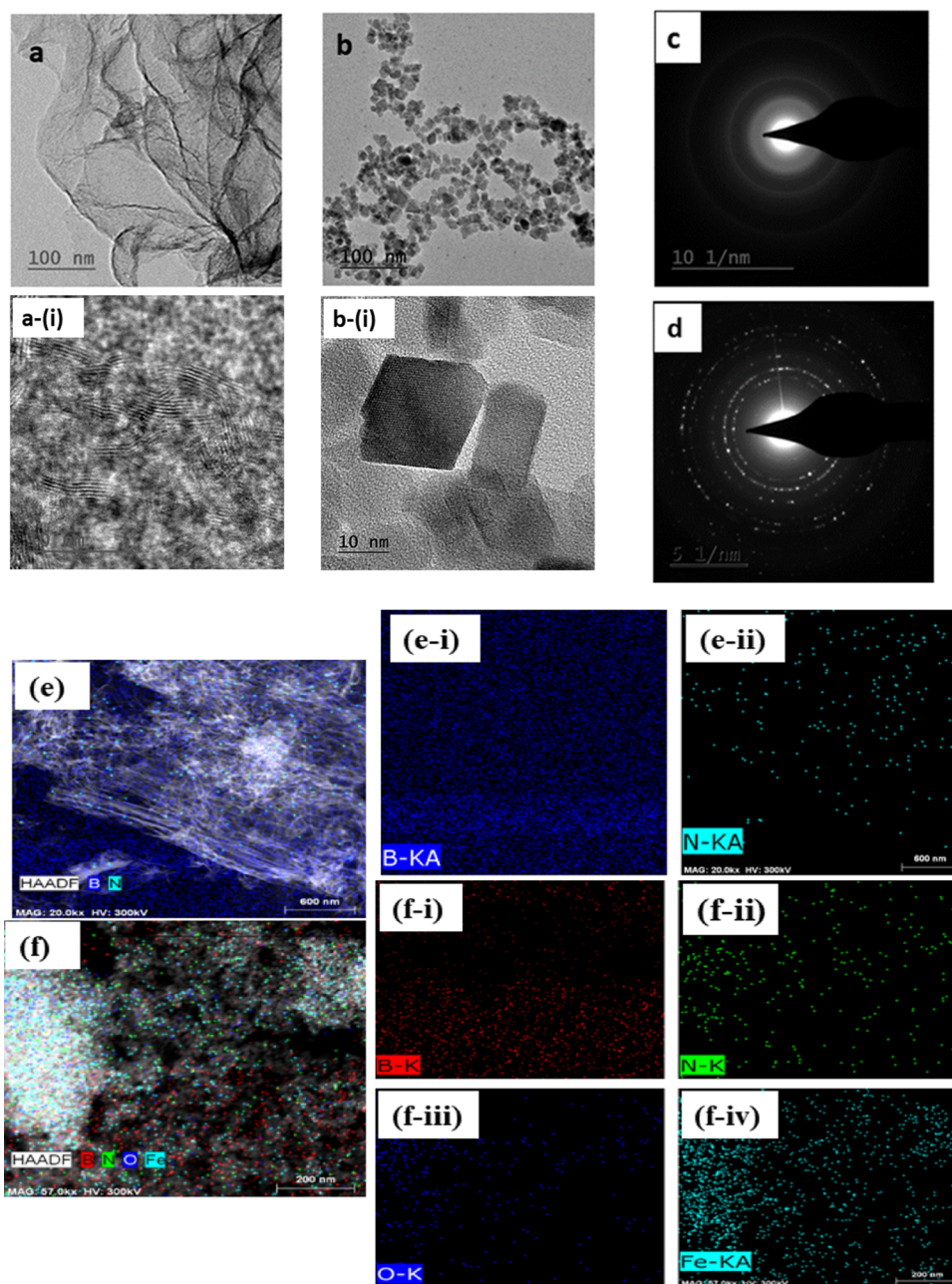


**Figure 3.** HRTEM images of (a) BNNSs and (b) BNNS-Fe<sub>3</sub>O<sub>4</sub> nanocomposite. SAED patterns of (c) BNNSs and (d) BNNS-Fe<sub>3</sub>O<sub>4</sub> nanocomposite. Elemental mapping images of (e) BNNSs: (e-i) boron and (e-ii) nitrogen and (f) BNNS-Fe<sub>3</sub>O<sub>4</sub> nanocomposite: (f-i) boron, (f-ii) nitrogen, (f-iii) oxygen, and (f-iv) Fe.

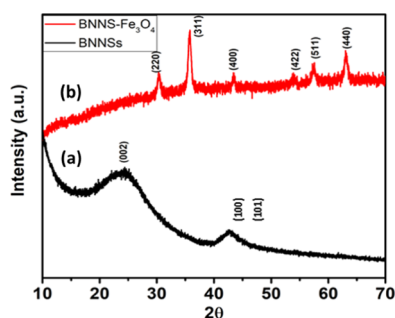


**Figure 4.** XRD pattern of (a) BNNSs and (b) BNNS-Fe<sub>3</sub>O<sub>4</sub> nanocomposite.

saturation of available active sites on the adsorbent. The kinetic data were analyzed by PFO and PSO models, and the corresponding parameters of the adsorbents are listed in Table 1. The kinetics rate constants  $k_1$  and  $k_2$  were determined from eqs 2 and 3, respectively. The PSO kinetic model showed a higher correlation ( $R^2 = 0.99$ ) than the PFO ( $R^2 = 0.97$ ) kinetic model. Consequently, it can be assumed that both the adsorbents followed this model.

**3.3.4. Adsorption Isotherms.** To determine the effect of the initial concentration of As(III) on the adsorption capacity, an adsorption isotherm study was performed (see Figure 11). Langmuir and Freundlich models were used to analyze the experimental data. The Langmuir isotherm model assumes the monolayer adsorption behavior of the adsorbent.<sup>49</sup> On the

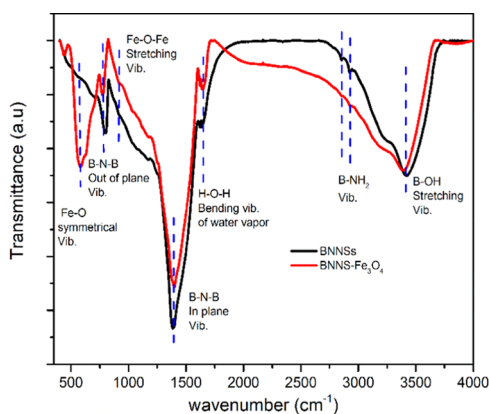


Figure 5. FTIR spectra of BNNSs and BNNS-Fe<sub>3</sub>O<sub>4</sub> nanocomposite.

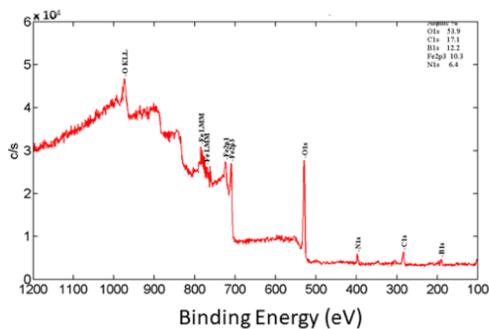


Figure 6. Percentage composition of each element on BNNS-Fe<sub>3</sub>O<sub>4</sub> nanocomposite.

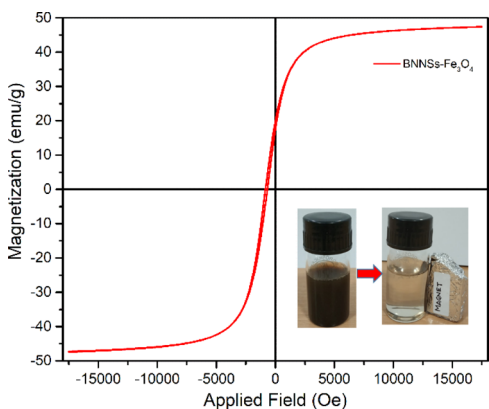


Figure 7. M–H curve of BNNS-Fe<sub>3</sub>O<sub>4</sub> nanocomposite; the inset image shows the separation of nanocomposite with the help of a magnet.

other hand, the Freundlich model represents the multilayer adsorption behavior of the adsorbent.<sup>43</sup> The experimental value of the As(III) adsorption capacity shown by BNNSs and the nanocomposite were obtained as 8.50 and 26.70 mg g<sup>-1</sup>, respectively. The high correlation ( $R^2 = 0.98$ ) in the case of BNNSs implies that the adsorption of As(III) is dominated by the Freundlich isotherm model. Conversely, the Langmuir isotherm model governs As(III) adsorption in the case of BNNS-Fe<sub>3</sub>O<sub>4</sub> as indicated by its correlation coefficient ( $R^2 = 0.96$ ). All of the calculated adsorption parameters are listed in Table 2. The maximum adsorption capacity of BNNS-Fe<sub>3</sub>O<sub>4</sub> calculated through the Langmuir isotherm model was found to be 30.30 mg g<sup>-1</sup>. This nearly 4 times enhancement is in line

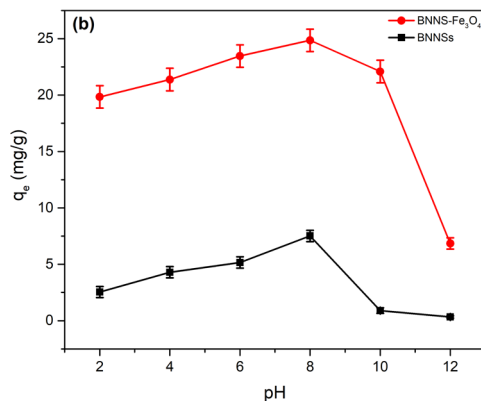
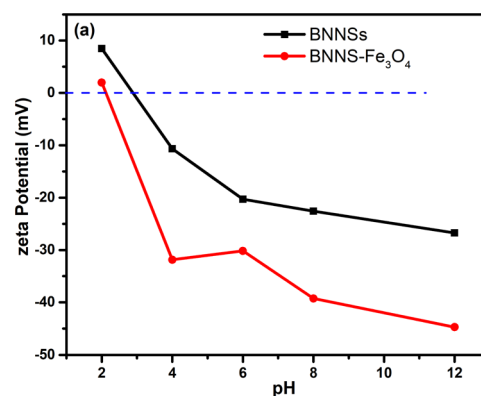


Figure 8. (a)  $\zeta$ -Potential values of BNNSs and BNNS-Fe<sub>3</sub>O<sub>4</sub> nanocomposite. (b) Effect of pH on the adsorption capacities of BNNSs and BNNS-Fe<sub>3</sub>O<sub>4</sub> nanocomposite.

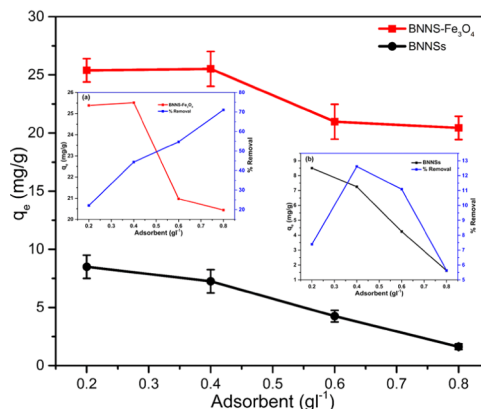
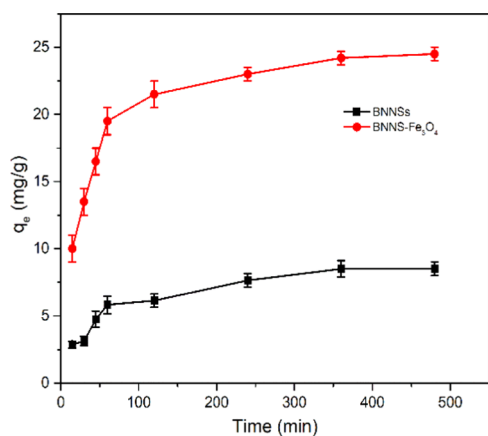


Figure 9. Effect of adsorbent dose on the adsorption capacities of BNNSs and BNNS-Fe<sub>3</sub>O<sub>4</sub> nanocomposite (insets (a) and (b) show adsorption capacity along with % removal).

with the theoretical simulations performed by DFT calculations.

**3.3.5. Possible Mechanism of As(III) Adsorption.** The good performance of BNNS-Fe<sub>3</sub>O<sub>4</sub> is attributed to the As(III) adsorption on the iron oxide surface through the inner-sphere ligand-exchange mechanism.<sup>50–52</sup> This is followed by mono-dentate and outer-sphere complex formation that are expressed by eqs 6 and 7.<sup>44</sup> Figure 12 shows the presence of As(III) in the elemental distribution mapping of BNNS-Fe<sub>3</sub>O<sub>4</sub> nanocomposite after adsorption. This reveals the bonding of As(III) with the nanocomposite. Further, the FTIR spectrum shows a peak at 773.20 cm<sup>-1</sup>, which is indicative of the stretching vibration



**Figure 10.** Effect of contact time on the adsorption capacities of BNNSs and BNNS-Fe<sub>3</sub>O<sub>4</sub> nanocomposite.

**Table 1. Pseudo-First-Order and Pseudo-Second-Order Kinetic Parameters**

kinetic model	parameters	BNNSs	BNNS-Fe <sub>3</sub> O <sub>4</sub>
pseudo-first-order	$q_{e,cal}$ (mg g <sup>-1</sup> )	6.18	12.72
	$k_1$ (min <sup>-1</sup> )	$9.1 \times 10^{-3}$	$10.7 \times 10^{-3}$
	$R^2$	0.977	0.972
pseudo-second-order	$q_{e,cal}$ (mg g <sup>-1</sup> )	9.29	25.77
	$K_2$ (g mg <sup>-1</sup> min <sup>-1</sup> )	$1.93 \times 10^{-3}$	$1.88 \times 10^{-3}$
	$R^2$	0.995	0.999

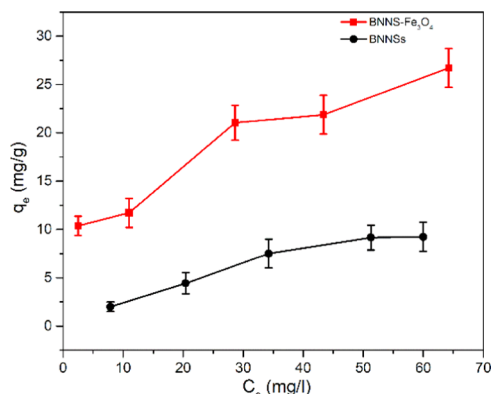


**Figure 11.** Adsorption isotherm of BNNSs and BNNS-Fe<sub>3</sub>O<sub>4</sub> nanocomposite.

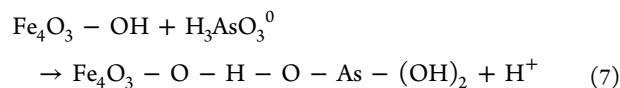
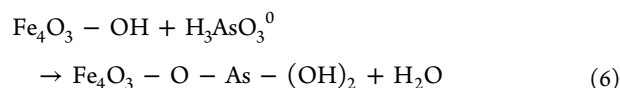
**Table 2. Adsorption Isotherm Parameters for BNNSs and BNNS-Fe<sub>3</sub>O<sub>4</sub>**

	parameters	BNNSs	BNNS-Fe <sub>3</sub> O <sub>4</sub>
experimental adsorption capacity	$q_{e,exp}$ (mg g <sup>-1</sup> )	8.50	26.70
Langmuir isotherm model	$q_{e,cal}$ (mg g <sup>-1</sup> )	<sup>a</sup>	30.30
	$K_L$ (L mg <sup>-1</sup> )	<sup>a</sup>	0.086
	$R^2$	0.900	0.957
Freundlich isotherm model	$K_F$ (mg <sup>1-n</sup> L <sup>n</sup> g <sup>-1</sup> )	0.411	<sup>a</sup>
	$n$	1.272	<sup>a</sup>
	$R^2$	0.983	0.899

<sup>a</sup>Not calculated because the adsorbent did not follow the corresponding isotherm model.

of the As–O bond (see Figure 13). This also confirms the adsorption of As(III) through the inner-sphere ligand-

exchange mechanism. Therefore, both the analyses support the mechanism of inner-sphere complex formation that is in agreement with the literature.



To investigate further, the pristine and arsenic adsorbed samples were analyzed by Raman spectroscopy. The Raman spectrum (see Figure 14) clearly shows the presence of a peak at 380 cm<sup>-1</sup>. This peak corresponds to the presence of As–(OH) symmetric stretching bonds.<sup>53</sup> Moreover, the survey and narrow spectra of As 3d in Figure 15 confirms the presence of As(III) in the adsorbed sample. The broad peak of As 3d depicts the presence of As(III) and As(V) at 43.20 and 44.6 eV, respectively.<sup>52,54</sup> The presence of As(V) in the adsorbed sample is attributed to the oxidation of As(III) during the adsorption of As(III) on the BNNS-Fe<sub>3</sub>O<sub>4</sub> nanocomposite.<sup>52</sup>

**3.4. Adsorption Thermodynamics.** In this study, the effect of temperature too has been investigated since it also plays a significant role in adsorption. Accordingly, the adsorption experiments were carried out at three different temperatures (25, 35, and 45 °C). Further, the thermodynamic parameters such as change in Gibbs free energy change ( $\Delta G^0$ ), enthalpy change ( $\Delta H^0$ ), and entropy change ( $\Delta S^0$ ) were evaluated by the following equations<sup>55–57</sup>

$$K_c = q_e / C_e \quad (8)$$

$$\Delta G^0 = -RT \ln K_c \quad (9)$$

$$\Delta G^0 = \Delta H^0 - T\Delta S^0 \quad (10)$$

where  $K_c$  is the equilibrium constant,  $q_e$  is the amount of solute adsorbed on the adsorbent,  $C_e$  is the remaining concentration of the adsorbate at equilibrium in the solution,  $T$  is the temperature in Kelvin, and  $R$  is the universal gas constant. The slope and intercept of the  $\Delta G^0$  vs  $T$  plot in Figure 16 were used to calculate  $\Delta H^0$  and  $\Delta S^0$ , respectively. The calculated values of  $\Delta G^0$ ,  $\Delta H^0$ , and  $\Delta S^0$  are listed in Table 3. One can see that  $\Delta G^0$  decreases from  $-15.35$  to  $-16.92$  (kJ mol<sup>-1</sup>) with an increase in temperature for BNNS-Fe<sub>3</sub>O<sub>4</sub>. This indicates that the adsorption is more favorable at a high temperature for BNNS-Fe<sub>3</sub>O<sub>4</sub>. On the other hand,  $\Delta G^0$  increases from  $-12.47$  to  $-9.05$  (kJ mol<sup>-1</sup>) for BNNSs, which means that the adsorption of As(III) on BNNSs is unfavorable at higher temperatures. Positive ( $+7.999$  kJ mol<sup>-1</sup>) and negative ( $-13.099$  kJ mol<sup>-1</sup>) values of  $\Delta H^0$  for BNNS-Fe<sub>3</sub>O<sub>4</sub> and BNNSs indicate the endothermic and exothermic behavior of the reaction, respectively. The  $\Delta S^0$  values for BNNSs and BNNS-Fe<sub>3</sub>O<sub>4</sub> are obtained as  $+1708.0$  and  $-78.0$  J mol<sup>-1</sup> K<sup>-1</sup>, respectively. The negative value of  $\Delta S^0$  in the case of BNNS-Fe<sub>3</sub>O<sub>4</sub> implies its affinity for As(III).<sup>58</sup>

**3.5. Regeneration Study.** From the pH study, it was found that the adsorption capacity decreases continuously when the pH increases from 8.0 to higher values. Therefore, to regenerate the As(III)-adsorbed adsorbent (BNNS-Fe<sub>3</sub>O<sub>4</sub>), it was further added in 1.0 M NaOH solution for 24 h. For the regeneration analysis. Three samples, named as pristine, after adsorption, and after regeneration, were examined by FTIR

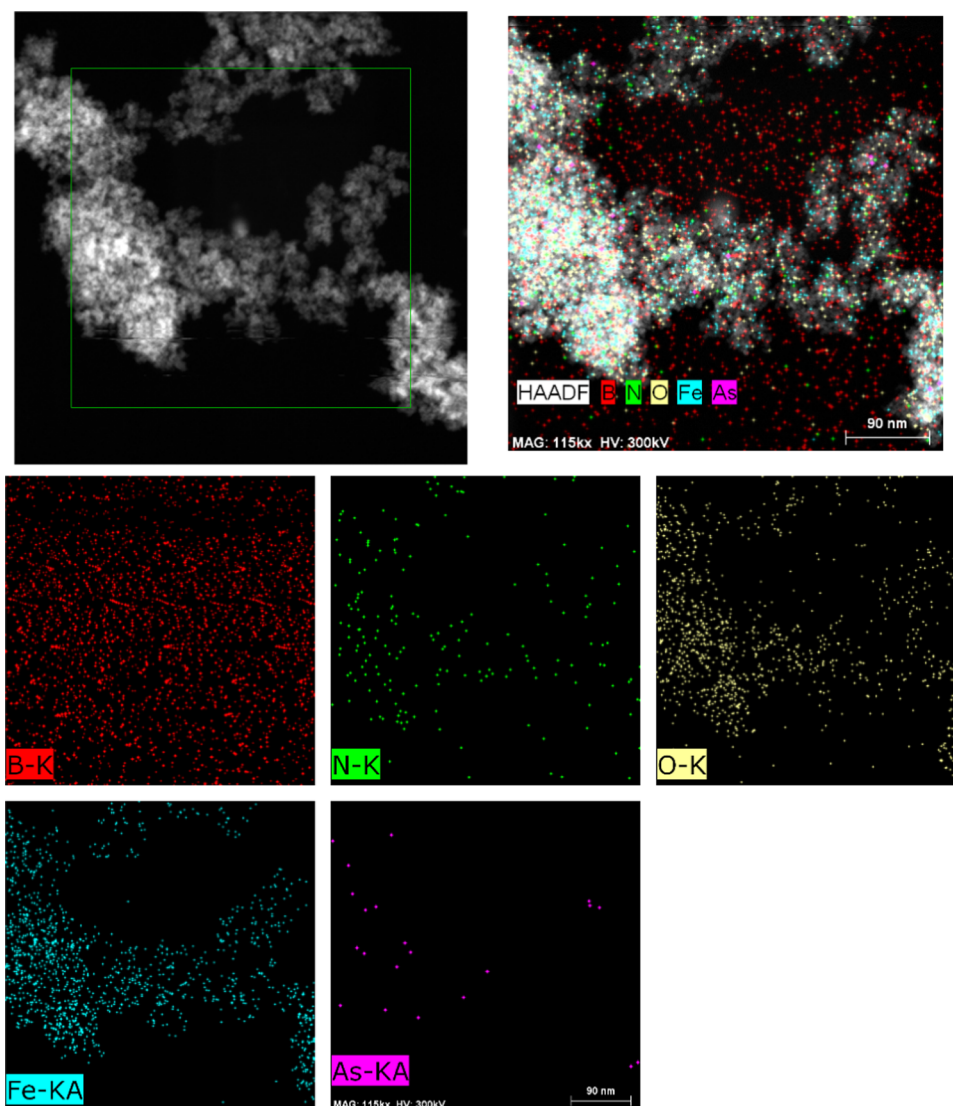


**Figure 12.** TEM image and energy-dispersive spectrometry (EDS) mapping of BNNS-Fe<sub>3</sub>O<sub>4</sub> after As(III) adsorption.

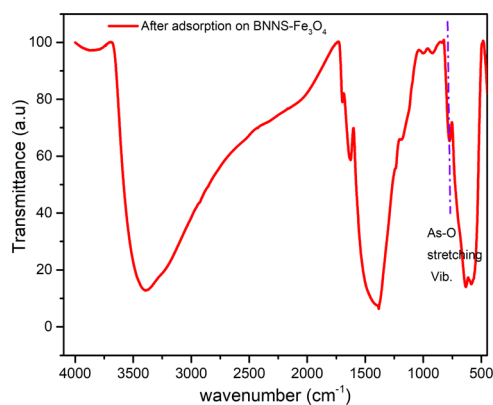


**Figure 13.** FTIR spectra of BNNS-Fe<sub>3</sub>O<sub>4</sub> after As(III) adsorption.

spectroscopy. The corresponding spectra (see Figure 17a) of the sample after adsorption showed a peak at 835 cm<sup>-1</sup>, which corresponds to the As–O stretching vibration.<sup>52</sup> The same peak was missing in the pristine and after regeneration in samples. Therefore, this result confirms the successful regeneration of BNNS-Fe<sub>3</sub>O<sub>4</sub>. The regenerated samples were

further examined for the adsorption capacity. Figure 17b shows the adsorption capacity of the adsorbent after adsorption–desorption–regeneration cycle. It was found that the adsorbent retained the same adsorption capacity for five cycles.

**3.6. Application of BNNS-Fe<sub>3</sub>O<sub>4</sub> Nanocomposite for Higher Concentrations of As(III) ions.** Finally, with the aim of testing the efficacy of the synthesized adsorption in real samples, we have considered the Ballia district in the state of Uttar Pradesh of India where severe health problems as a result of high concentration of As ions (as high as 218 ppb As(III)) in potable water have been reported.<sup>59</sup> Therefore, this range of As ions has been used to test the synthesized adsorbent. The results in Table 4 show the potential of the synthesized BNNSs-Fe<sub>3</sub>O<sub>4</sub> nanocomposite as an adsorbent for As levels well above the WHO guideline. Further, it has been demonstrated that the higher concentrations of As(III) can be brought to the drinking level by increasing the temperature. At room temperature (25 °C), low concentrations of As(III) starting from 68.79 to 134.13 ppb can be successfully reduced to 2.65 and 2.67 ppb, respectively by applying the synthesized nanocomposite. However, it fails to bring it down to the safe drinking limit at initial concentrations of 351.30 ppb and



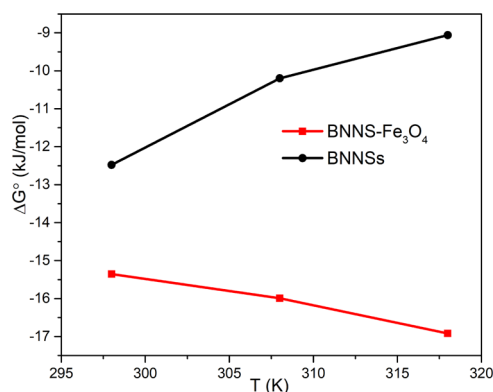


**Figure 16.** Plot of Gibbs free-energy change ( $\Delta G^0$ ) versus temperature for exothermic (BNNSSs) and endothermic (BNNS- $\text{Fe}_3\text{O}_4$ ) processes.

magnetic nanoparticle-functionalized graphene and graphene oxide and showed better adsorption capacity than most of the adsorbents. There are a few studies that have reported a higher adsorption capacity than the current study.<sup>13,60</sup> However, they have not reported about the regeneration and separation property of the adsorbents. Some of the other studies report a high adsorption capacity at a high initial concentration range, i.e., 1–250 ppm, of As(III).<sup>16</sup> However, this concentration range of As(III) is not practically available in many parts of the world. The As(III) contamination is found to be below 1 ppm in the majority of the cases.<sup>59,61</sup> Therefore, it is also important to study the adsorption behavior of the adsorbent at this concentration range, which has been done in this study. In sum, this study demonstrates the potential of BNNS- $\text{Fe}_3\text{O}_4$  nanocomposites as novel adsorbents for As(III) removal from water.

#### 4. CONCLUSIONS

This study presented the synthesis of BNNSSs and BNNS- $\text{Fe}_3\text{O}_4$  nanocomposite with SBET values of BNNSSs and BNNS- $\text{Fe}_3\text{O}_4$  of 1801.9 and 179.5  $\text{m}^2 \text{g}^{-1}$ , respectively. Further, their performance as adsorbents for As(III) removal from contaminated water was studied with various adsorption parameters that included pH, adsorption time, dosage rate, and the effect of the initial concentration of As(III). It was found through the pH study that the maximum adsorption could be achieved at pH = 8. The thermodynamic study showed the exothermic and endothermic nature of BNNSSs and BNNS- $\text{Fe}_3\text{O}_4$  nanocomposite, respectively. Additionally, the kinetic analysis showed that the As(III) adsorption on both of them followed the PSO kinetic model. The adsorption isotherms of BNNSSs fitted well with the Freundlich model, while it correlated well with the Langmuir model in the case of BNNS- $\text{Fe}_3\text{O}_4$ . The maximum adsorption capacity of BNNSSs was found to be 8.5  $\text{mg g}^{-1}$ , while it was 30.3  $\text{mg g}^{-1}$  in the case of BNNS- $\text{Fe}_3\text{O}_4$ . This nearly 4-fold increase in the

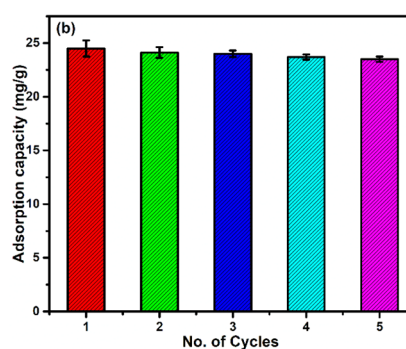
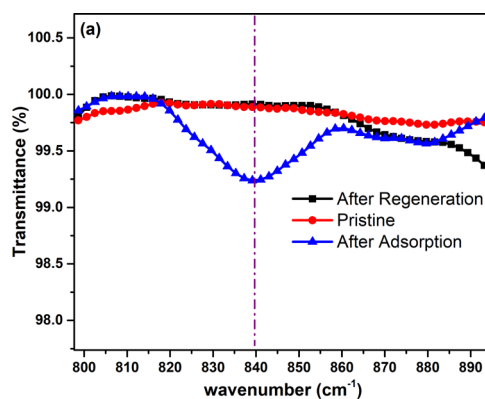


**Figure 17.** (a) Regeneration and (b) recycling results of As(III)-adsorbed samples.

**Table 4.** As(III) Concentration after Adsorption on BNNSSs- $\text{Fe}_3\text{O}_4$  (Experimental Conditions: pH, 8.0; Dose of Adsorbent, 0.4  $\text{g l}^{-1}$ ; Temp, 25 and 35 °C)

25 °C		35 °C	
$C_0$ (before adsorption, ppb)	$C_e$ (after adsorption, ppb)	$C_0$ (before adsorption, ppb)	$C_e$ (after adsorption, ppb)
68.79	2.65	140.18	2.05
134.13	2.67	165.05	2.16
351.30	19.63	347.05	5.95
567.86	46.48	566.42	10.29

adsorption capacity is mainly due to the enhanced binding affinity of  $\text{As}(\text{OH})_3$  on the BNNS- $\text{Fe}_3\text{O}_4$  nanocomposite, as revealed by the DFT calculations. The synthesized BNNS- $\text{Fe}_3\text{O}_4$  nanocomposite was able to reduce 134 ppb of As(III) to 2.67 ppb at room temperature (25 °C). With an increase in the temperature to 35 °C, the synthesized nanocomposite could decrease the level of As(III) from up to 556 to 10.29 ppb that it is very close to the limit recommended by WHO. Since the nanocomposite exhibited superparamagnetic behavior at room temperature, its separation from water was achieved quite easily. Moreover, the synthesized adsorbent showed regeneration behavior. Hence, the synthesized nanocomposite

**Table 3.** Thermodynamic Parameters for the Adsorption of As(III) on BNNSSs and BNNS- $\text{Fe}_3\text{O}_4$

temp. (K)	BNNSSs			BNNS- $\text{Fe}_3\text{O}_4$		
	$\Delta G^0$ ( $\text{kJ mol}^{-1}$ )	$\Delta H^0$ ( $\text{kJ mol}^{-1}$ )	$\Delta S^0$ ( $\text{J mol}^{-1} \text{K}^{-1}$ )	$\Delta G^0$ ( $\text{kJ mol}^{-1}$ )	$\Delta H^0$ ( $\text{kJ mol}^{-1}$ )	$\Delta S^0$ ( $\text{J mol}^{-1} \text{K}^{-1}$ )
298	-12.47	-13.099	1708	-15.35	7.999	-78
308	-10.17			-15.99		
318	-9.05			-16.92		

Table 5. Comparison of Maximum As(III) Adsorption Capacities Reported by Different Adsorbents

adsorbent	pH	initial conc./conc. range (ppm)	adsorption capacity (mg g <sup>-1</sup> )	regeneration	magnetic separation	refs
magnetite-reduced graphene oxide composites	7.0	3–7	13.10	not reported	reported	18
mesoporous silica coated with Fe and Al oxides	8.0	0–50	13.30	not reported	not reported	21
magnetic activated carbon nanotubes	5.5	0.5–11	8.13	not reported	reported	20
cupric oxide nanoparticles	8.0	0.1–100	26.90	not reported	not reported	62
graphene aerogels decorated with $\alpha$ -FeOOH nanoparticles	9.0	1–16	13.42	not reported	not reported	22
magnetic CuO–Fe <sub>3</sub> O <sub>4</sub> nanoparticles	7.0	0.1–50	118.11	not reported	reported	60
magnetic ordered mesoporous Fe/Ce bimetal oxides (OMICs)	7.0	1–150	281.34	reported	reported	16
microscale dialdehyde cellulose–cysteine (MDAC–cys) fiber	7.0	50–250	344.82	not reported	not reported	13
nanoscale dialdehyde cellulose–cysteine (NDAC–cys) fiber	7.0	50–250	357.14	not reported	not reported	
iron oxide–multiwalled carbon nanotube hybrid	4.0	NA	1.70	not reported	not reported	19
nano zero-valent iron on activated carbon	6.5	NA	18.19	reported	not reported	49
functionalized synthetic graphite	7.5–8.0	0.1 to 50	18.80	reported	not reported	63
ZMA (Sonora)	4.0	0.1–4	0.01	not reported	not reported	64
manganese-incorporated iron(III) oxide–graphene nanocomposite	7.0		14.42	not reported	reported	65
Fe <sub>2</sub> O <sub>3</sub> @C		0.2–30	29.40	reported	reported	66
Fe/Mn-HDTMA kaolin	6.5 ± 0.2	0.5–30	7.99	reported	not reported	67
MBC	7.0	1–12	5.06	not reported	not reported	68
MNP-PCP	8.0	25–150	13.86	reported	reported	69
Fe/Cu nanoparticles	7.0	0.1–5	19.68	not reported	not reported	70
surfactant modified kaolin clay	6.0 ± 0.5	1–30	2.33	reported	not reported	71
iron nanoparticle-modified	3.0	50–250	24.2	not reported	not reported	72
humic acid-grafted MNPs	6.6	0.1–10	12.2	not reported	reported	15
magnetite nanoparticles	5.0	3.75–75	16.6	not reported	reported	73
BNNS-Fe <sub>3</sub> O <sub>4</sub>	8.0	6–70	30.30	reported	reported	this study

demonstrates its suitability as a promising candidate for the treatment of As(III) ions from polluted water.

## ■ ASSOCIATED CONTENT

### ■ Supporting Information

The Supporting Information is available free of charge at <https://pubs.acs.org/doi/10.1021/acsomega.9b04295>.

FESEM, BET images; N<sub>2</sub> adsorption–desorption isotherm; and pore size distribution of BNNSs and BNNS-Fe<sub>3</sub>O<sub>4</sub> (PDF)

## ■ AUTHOR INFORMATION

### Corresponding Authors

Jayant K. Singh – Department of Chemical Engineering, Indian Institute of Technology Kanpur, Kanpur 208016, India; [orcid.org/0000-0001-8056-2115](https://orcid.org/0000-0001-8056-2115); Email: [jayantks@iitk.ac.in](mailto:jayantks@iitk.ac.in)

Niraj Sinha – Department of Mechanical Engineering, Indian Institute of Technology Kanpur, Kanpur 208016, India; [orcid.org/0000-0001-6600-9313](https://orcid.org/0000-0001-6600-9313); Phone: (0512) 6797196; Email: [nsinha@iitk.ac.in](mailto:nsinha@iitk.ac.in); Fax: (0512) 6797408

## Authors

Raghubeer S. Bangari – Department of Mechanical Engineering, Indian Institute of Technology Kanpur, Kanpur 208016, India; [orcid.org/0000-0001-6828-7456](https://orcid.org/0000-0001-6828-7456)

Vivek K. Yadav – Department of Chemical Engineering, Indian Institute of Technology Kanpur, Kanpur 208016, India; [orcid.org/0000-0002-9142-4567](https://orcid.org/0000-0002-9142-4567)

Complete contact information is available at: <https://pubs.acs.org/10.1021/acsomega.9b04295>

## Notes

The authors declare no competing financial interest.

## ■ ACKNOWLEDGMENTS

The authors acknowledge support from Department of Science and Technology, Government of India, under Water Technology Initiative [project number DST/TM/WTI/2K15/112]. V.K.Y. acknowledges support of MHRD, India [Sanction number: F. NO. 5-6/2013 TS-VII].

## ■ REFERENCES

- (1) Ministry Of Water Resources River Development and Ganga Rejuvenation. *Occurrence Of High Arsenic Content In Ground Water Committee On Estimates (2014-15)*; 2014.
- (2) Sinha, N. Nanomaterials-Based Solutions: Detection of Arsenic in Contaminated Water. *IEEE Nanotechnol. Mag.* **2014**, *8*, 17–23.
- (3) Ghuha Mazumder, D. N. Chronic Arsenic Toxicity & Human Health. *Indian J. Med. Res.* **2008**, *128*, 436–447.
- (4) Sarkar, A.; Paul, B. The Global Menace of Arsenic and Its Conventional Remediation - A Critical Review. *Chemosphere* **2016**, *158*, 37–49.
- (5) Smedley, P. L.; Kinniburgh, D. G. A Review of the Source, Behaviour and Distribution of Arsenic in Natural Waters. *Appl. Geochem.* **2002**, *17*, 517–568.
- (6) Rahman, M. N.; Ng, J. C.; Naidu, R. Chronic Exposure of Arsenic via Drinking Water and Its Adverse Health Impacts on Humans. *Environ. Geochem. Health* **2009**, *31*, 189–200.
- (7) Korte, N. E.; Fernando, Q. A Review of Arsenic (III) in Groundwater. *Crit. Rev. Environ. Control* **1991**, *21*, 1–39.
- (8) Mondal, P.; Bhowmick, S.; Chatterjee, D.; Figoli, A.; Van der Bruggen, B. Remediation of Inorganic Arsenic in Groundwater for Safe Water Supply: A Critical Assessment of Technological Solutions. *Chemosphere* **2013**, *92*, 157–170.
- (9) Kumar, R.; Patel, M.; Singh, P.; Bundschuh, J.; Pittman, C. U.; Trakal, L.; Mohan, D. Emerging Technologies for Arsenic Removal from Drinking Water in Rural and Peri-Urban Areas: Methods, Experience From, and Options for Latin America. *Sci. Total Environ.* **2019**, *694*, 133427.
- (10) Nicomel, N. R.; Leus, K.; Folens, K.; Van Der Voort, P.; Du Laing, G. Technologies for Arsenic Removal from Water: Current Status and Future Perspectives. *Int. J. Environ. Res. Public Health* **2015**, *13*, 1–24.
- (11) Habuda-Stanić, M.; Nujčić, M. Arsenic Removal by Nanoparticles: A Review. *Environ. Sci. Pollut. Res.* **2015**, *22*, 8094–8123.
- (12) Pathan, S.; Bose, S. Arsenic Removal Using “green” Renewable Feedstock-Based Hydrogels: Current and Future Perspectives. *ACS Omega* **2018**, *3*, 5910–5917.
- (13) Chen, H.; Sharma, S. K.; Sharma, P. R.; Yeh, H.; Johnson, K.; Hsiao, B. S. Arsenic(III) Removal by Nanostructured Dialdehyde Cellulose-Cysteine Microscale and Nanoscale Fibers. *ACS Omega* **2019**, *4*, 22008–22020.
- (14) Meng, K.; Wu, X.; Zhang, X.; Su, S.; Huang, Z.; Min, X.; Liu, Y.; Fang, M. Efficient Adsorption of the Cd(II) and As(V) Using Novel Adsorbent Ferrihydrite/Manganese Dioxide Composites. *ACS Omega* **2019**, *4*, 18627–18636.
- (15) Rashid, M.; Sterbinsky, G. E.; Pinilla, M. Á.G.; Cai, Y.; O’Shea, K. E. Kinetic and Mechanistic Evaluation of Inorganic Arsenic Species Adsorption onto Humic Acid Grafted Magnetite Nanoparticles. *J. Phys. Chem. C* **2018**, *122*, 13540–13547.
- (16) Wen, Z.; Lu, J.; Zhang, Y.; Cheng, G.; Huang, S.; Chen, J.; Xu, R.; Ming, Y. an.; Wang, Y.; Chen, R. Facile Inverse Micelle Fabrication of Magnetic Ordered Mesoporous Iron Cerium Bimetal Oxides with Excellent Performance for Arsenic Removal from Water. *J. Hazard. Mater.* **2020**, *383*, No. 121172.
- (17) Hao, L.; Liu, M.; Wang, N.; Li, G. A Critical Review on Arsenic Removal from Water Using Iron-Based Adsorbents. *RSC Adv.* **2018**, *8*, 39545–39560.
- (18) Chandra, V.; Park, J.; Chun, Y.; Lee, J. W.; Hwang, I. C.; Kim, K. S. Water-Dispersible Magnetite-Reduced Graphene Oxide Composites for Arsenic Removal. *ACS Nano* **2010**, *4*, 3979–3986.
- (19) Addo Ntim, S.; Mitra, S. Removal of Trace Arsenic to Meet Drinking Water Standards Using Iron Oxide Coated Multiwall Carbon Nanotubes. *J. Chem. Eng. Data* **2011**, *56*, 2077–2083.
- (20) Ma, J.; Zhu, Z.; Chen, B.; Yang, M.; Zhou, H.; Li, C.; Yu, F.; Chen, J. One-Pot, Large-Scale Synthesis of Magnetic Activated Carbon Nanotubes and Their Applications for Arsenic Removal. *J. Mater. Chem. A* **2013**, *1*, 4662–4666.
- (21) Glocheux, Y.; Albadarin, A. B.; Galán, J.; Oyedoh, E.; Mangwandi, C.; Gérente, C.; Allen, S. J.; Walker, G. M. Adsorption Study Using Optimised 3D Organised Mesoporous Silica Coated with Fe and Al Oxides for Specific As(III) and As(V) Removal from Contaminated Synthetic Groundwater. *Microporous Mesoporous Mater.* **2014**, *198*, 101–114.
- (22) Andjelkovic, I.; Tran, D. N. H.; Kabiri, S.; Azari, S.; Markovic, M.; Losic, D. Graphene Aerogels Decorated with  $\alpha$ -FeOOH Nanoparticles for Efficient Adsorption of Arsenic from Contaminated Waters. *ACS Appl. Mater. Interfaces* **2015**, *7*, 9758–9766.
- (23) Su, H.; Ye, Z.; Hmidi, N. High-Performance Iron Oxide-Graphene Oxide Nanocomposite Adsorbents for Arsenic Removal. *Colloids Surf., A* **2017**, *522*, 161–172.
- (24) Khatamian, M.; Khodakarampoor, N.; Saket-Oskoui, M. Efficient Removal of Arsenic Using Graphene-Zeolite Based Composites. *J. Colloid Interface Sci.* **2017**, *498*, 433–441.
- (25) Humphrey, W.; Dalke, A.; Schulten, K. VMD: Visual Molecular Dynamics. *J. Mol. Graphics* **1996**, *14*, 33–38.
- (26) Marcus, D. H.; Curtis, D. E.; Lonie, D. C.; Vandermeersch, T.; Zurek, E.; Hutchison, G. R. Avogadro: An Advanced Semantic Chemical Editor. *J. Cheminformatics* **2012**, *4*, No. 17.
- (27) Giannozzi, P.; Baroni, S.; Bonini, N.; Calandra, M.; Car, R.; Cavazzoni, C.; Ceresoli, D.; Chiarotti, G. L.; Cococcioni, M.; Dabo, I.; et al. QUANTUM ESPRESSO: A Modular and Open-Source Software Project for Quantum Simulations of Materials. *J. Phys.: Condens. Matter* **2009**, *21*, No. 395502.
- (28) Perdew, J. P.; Burke, K.; Ernzerhof, M. Generalized Gradient Approximation Made Simple. *Phys. Rev. Lett.* **1996**, *77*, 3865–3868.
- (29) Rappe, A. M.; Rabe, K. M.; Kaxiras, E.; Joannopoulos, J. D. Optimized Pseudopotentials. *Phys. Rev. B* **1990**, *41*, 1227–1230.
- (30) Monkhorst, H. J.; Pack, J. D. Special Points for Brillouin-Zone Integrations. *Phys. Rev. B* **1976**, *13*, 5188–5192.
- (31) Grimme, S.; Antony, J.; Ehrlich, S.; Krieg, H. A Consistent and Accurate Ab Initio Parametrization of Density Functional Dispersion Correction (DFT-D) for the 94 Elements H-Pu. *J. Chem. Phys.* **2010**, *132*, No. 154104.
- (32) Bangari, R. S.; Singh, A. K.; Namsani, S.; Singh, J. K.; Sinha, N. Magnetite-Coated Boron Nitride Nanosheets for the Removal of Arsenic(V) from Water. *ACS Appl. Mater. Interfaces* **2019**, *11*, 19017–19028.
- (33) Nag, A.; Raidongia, K.; Hembram, K. P. S. S.; Datta, R.; Waghmare, U. V.; Rao, C. N. R. Graphene Analogues of BN: Novel Synthesis and Properties. *ACS Nano* **2010**, *4*, 1539–1544.
- (34) Kumari, M.; Pittman, C. U.; Mohan, D. Heavy Metals [Chromium (VI) and Lead (II)] Removal from Water Using Mesoporous Magnetite (Fe<sub>3</sub>O<sub>4</sub>) Nanospheres. *J. Colloid Interface Sci.* **2015**, *442*, 120–132.
- (35) Andersson, K. I.; Eriksson, M.; Norgren, M. Removal of Lignin from Wastewater Generated by Mechanical Pulping Using Activated Charcoal and Fly Ash: Adsorption Isotherms and Thermodynamics. *Ind. Eng. Chem. Res.* **2011**, *50*, 7722–7732.
- (36) Nickson, R.; Sengupta, C.; Mitra, P.; Dave, S. N.; Banerjee, A. K.; Bhattacharya, A.; Basu, S.; Kakoti, N.; Moorthy, N. S.; Wasuja, M.; et al. Current Knowledge on the Distribution of Arsenic in Groundwater in Five States of India. *J. Environ. Sci. Health, Part A: Environ. Sci. Eng.* **2007**, *42*, 1707–1718.
- (37) Zhuang, L.; Zhang, W.; Zhao, Y.; Shen, H.; Lin, H.; Liang, J. Preparation and Characterization of Fe<sub>3</sub>O<sub>4</sub> Particles with Novel Nanosheets Morphology and Magnetochromatic Property by a Modified Solvothermal Method. *Sci. Rep.* **2015**, *5*, No. 9320.
- (38) Mou, Y.; Yang, H.; Xu, Z. Morphology, Surface Layer Evolution, and Structure-Dye Adsorption Relationship of Porous Fe<sub>3</sub>O<sub>4</sub> MNPs Prepared by Solvothermal/Gas Generation Process. *ACS Sustainable Chem. Eng.* **2017**, *5*, 2339–2349.
- (39) Liu, F.; Yu, J.; Ji, X.; Qian, M. Nanosheet-Structured Boron Nitride Spheres with a Versatile Adsorption Capacity for Water Cleaning. *ACS Appl. Mater. Interfaces* **2015**, *7*, 1824–1832.
- (40) Li, J.; Xiao, X.; Xu, X.; Lin, J.; Huang, Y.; Xue, Y.; Jin, P.; Zou, J.; Tang, C. Activated Boron Nitride as an Effective Adsorbent for Metal Ions and Organic Pollutants. *Sci. Rep.* **2013**, *3*, No. 3208.

- (41) Singh, K. P.; Singh, A. K.; Gupta, S.; Rai, P. Modeling and Optimization of Reductive Degradation of Chloramphenicol in Aqueous Solution by Zero-Valent Bimetallic Nanoparticles. *Environ. Sci. Pollut. Res.* **2012**, *19*, 2063–2078.
- (42) Yang, Y.; Chun, Y.; Sheng, G.; Huang, M. pH-Dependence of Pesticide Adsorption by Wheat-Residue-Derived Black Carbon. *Langmuir* **2004**, *20*, 6736–6741.
- (43) Guo, X.; Chen, F. Removal of Arsenic by Bead Cellulose Loaded with Iron Oxhydroxide from Groundwater. *Environ. Sci. Technol.* **2005**, *39*, 6808–6818.
- (44) Yoon, Y.; Park, W. K.; Hwang, T. M.; Yoon, D. H.; Yang, W. S.; Kang, J. W. Comparative Evaluation of Magnetite-Graphene Oxide and Magnetite-Reduced Graphene Oxide Composite for As(III) and As(V) Removal. *J. Hazard. Mater.* **2016**, *304*, 196–204.
- (45) Gupta, S. K.; Chen, K. Y. Arsenic Removal by Adsorption. *J. -Water Pollut. Control Fed.* **1978**, *50*, 493–506.
- (46) Maliyekkal, S. M.; Philip, L.; Pradeep, T. As(III) Removal from Drinking Water Using Manganese Oxide-Coated-Alumina: Performance Evaluation and Mechanistic Details of Surface Binding. *Chem. Eng. J.* **2009**, *153*, 101–107.
- (47) Yang, K.; Chen, B.; Zhu, L. Graphene-Coated Materials Using Silica Particles as a Framework for Highly Efficient Removal of Aromatic Pollutants in Water. *Sci. Rep.* **2015**, *5*, No. 11641.
- (48) Zhao, J.; Wang, Z.; Zhao, Q.; Xing, B. Adsorption of Phenanthrene on Multilayer Graphene as Affected by Surfactant and Exfoliation. *Environ. Sci. Technol.* **2014**, *48*, 331–339.
- (49) Zhu, H.; Jia, Y.; Wu, X.; Wang, H. Removal of Arsenic from Water by Supported Nano Zero-Valent Iron on Activated Carbon. *J. Hazard. Mater.* **2009**, *172*, 1591–1596.
- (50) Katsoyiannis, I. A.; Zouboulis, A. I. Removal of Arsenic from Contaminated Water Sources by Sorption onto Iron-Oxide Coated Polymeric Materials. *Water Res.* **2002**, *36*, 5141–5155.
- (51) Pena, M.; Meng, X.; Korfiatis, G. P.; Jing, C. Adsorption Mechanism of Arsenic on Nanocrystalline Titanium Dioxide. *Environ. Sci. Technol.* **2006**, *40*, 1257–1262.
- (52) Penke, Y. K.; Anantharaman, G.; et al. A Ternary Metal Oxide Adsorbent for Arsenic Adsorption in Aqueous Medium †. *RSC Adv.* **2016**, *6*, 55608–55617.
- (53) Goldberg, S.; Johnston, C. T. Mechanisms of Arsenic Adsorption on Amorphous Oxides Evaluated Using Macroscopic Measurements, Vibrational Spectroscopy, and Surface Complexation Modeling. *J. Colloid Interface Sci.* **2001**, *234*, 204–216.
- (54) Penke, Y. K.; Anantharaman, G.; Ramkumar, J.; Kar, K. K. Aluminum Substituted Cobalt Ferrite (Co-Al-Fe) Nano Adsorbent for Arsenic Adsorption in Aqueous Systems and Detailed Redox Behavior Study with XPS. *ACS Appl. Mater. Interfaces* **2017**, *9*, 11587–11598.
- (55) Anirudhan, T. S.; Radhakrishnan, P. G. Thermodynamics and Kinetics of Adsorption of Cu(II) from Aqueous Solutions onto a New Cation Exchanger Derived from Tamarind Fruit Shell. *J. Chem. Thermodyn.* **2008**, *40*, 702–709.
- (56) Kobiraj, R.; Gupta, N.; Kushwaha, A. K.; Chattopadhyaya, M. C. Determination of Equilibrium, Kinetic and Thermodynamic Parameters for the Adsorption of Brilliant Green Dye from Aqueous Solutions onto Eggshell Powder. *Indian J. Chem. Technol.* **2012**, *19*, 26–31.
- (57) Hu, Q.; Liu, Y.; Gu, X.; Zhao, Y. Adsorption Behavior and Mechanism of Different Arsenic Species on Mesoporous MnFe<sub>2</sub>O<sub>4</sub> Magnetic Nanoparticles. *Chemosphere* **2017**, *181*, 328–336.
- (58) He, J.; Hong, S.; Zhang, L.; Gan, F.; Ho, Y. Equilibrium and Thermodynamic Parameters of Methylene Blue onto Rectorite. *Fresenius Environ. Bull.* **2010**, *19*, 2651–2656.
- (59) Chauhan, V. S.; Nickson, R. T.; Chauhan, D.; Iyengar, L.; Sankaramakrishnan, N. Ground Water Geochemistry of Ballia District, Uttar Pradesh, India and Mechanism of Arsenic Release. *Chemosphere* **2009**, *75*, 83–91.
- (60) Sun, T.; Zhao, Z.; Liang, Z.; Liu, J.; Shi, W.; Cui, F. Efficient As(III) Removal by Magnetic CuO-Fe<sub>3</sub>O<sub>4</sub> Nanoparticles through Photo-Oxidation and Adsorption under Light Irradiation. *J. Colloid Interface Sci.* **2017**, *495*, 168–177.
- (61) Chakraborti, D.; Rahman, M. M.; Ahamed, S.; Dutta, R. N.; Pati, S.; Mukherjee, S. C. Arsenic Groundwater Contamination and Its Health Effects in Patna District (Capital of Bihar) in the Middle Ganga Plain, India. *Chemosphere* **2016**, *152*, 520–529.
- (62) Martinson, C. A.; Reddy, K. J. Adsorption of arsenic(III) and arsenic(V) by Cupric Oxide Nanoparticles. *J. Colloid Interface Sci.* **2009**, *336*, 406–411.
- (63) Uppal, H.; Hemlata; Tawale, J.; Singh, N. Zinc Peroxide Functionalized Synthetic Graphite: An Economical and Efficient Adsorbent for Adsorption of Arsenic (III) and (V). *J. Environ. Chem. Eng.* **2016**, *4*, 2964–2975.
- (64) Elizalde-González, M. P.; Mattusch, J.; Wennrich, R.; Morgenstern, P. Uptake of Arsenite and Arsenate by Clinoptilolite-Rich Tuffs. *Microporous Mesoporous Mater.* **2001**, *46*, 277–286.
- (65) Nandi, D.; Gupta, K.; Ghosh, A. K.; De Amitabha, D. A.; Banerjee, S.; Ghosh, U. C.; De, A.; Banerjee, S.; Ghosh, U. C. Manganese-Incorporated iron(III) Oxide-graphene Magnetic Nanocomposite: Synthesis, Characterization, and Application for the arsenic(III)-Sorption from Aqueous Solution. *J. Nanopart. Res.* **2012**, *14*, No. 1272.
- (66) Wu, Z.; Li, W.; Webley, P. A.; Zhao, D. General and Controllable Synthesis of Novel Mesoporous Magnetic Iron Oxide@carbon Encapsulates for Efficient Arsenic Removal. *Adv. Mater.* **2012**, *24*, 485–491.
- (67) Mudzielwana, R.; Gitari, M. W.; Ndungu, P. Enhanced As(III) and As(V) Adsorption From Aqueous Solution by a Clay Based Hybrid Sorbent. *Front. Chem.* **2020**, *7*, 1–10.
- (68) Navarathna, C. M.; Karunanayake, A. G.; Gunatilake, S. R.; Pittman, C. U.; Perez, F.; Mohan, D.; Mlsna, T. Removal of Arsenic(III) from Water Using Magnetite Precipitated onto Douglas Fir Biochar. *J. Environ. Manage.* **2019**, *250*, No. 109429.
- (69) Pholosi, A.; Naidoo, E. B.; Ofomaja, A. E. Enhanced Arsenic (III) Adsorption from Aqueous Solution by Magnetic Pine Cone Biomass. *Mater. Chem. Phys.* **2019**, *222*, 20–30.
- (70) Babae, Y.; Mulligan, C. N.; Rahaman, M. S. Removal of Arsenic (III) and Arsenic (V) from Aqueous Solutions through Adsorption by Fe/Cu Nanoparticles. *J. Chem. Technol. Biotechnol.* **2018**, *93*, 63–71.
- (71) Mudzielwana, R.; Gitari, M. W.; Ndungu, P. Performance Evaluation of Surfactant Modified Kaolin Clay in As(III) and As(V) Adsorption from Groundwater: Adsorption Kinetics, Isotherms and Thermodynamics. *Heliyon* **2019**, *5*, No. e02756.
- (72) Sarntanayoot, P.; Fuangswasdi, S.; Imyim, A. Iron Nanoparticle-Modified Water Treatment Residues for Adsorption of As(III) and As(V) and Their Cement-Based Solidification/stabilization. *Int. J. Environ. Sci. Technol.* **2019**, *16*, 4285–4292.
- (73) Liu, C. H.; Chuang, Y. H.; Chen, T. Y.; Tian, Y.; Li, H.; Wang, M. K.; Zhang, W. Mechanism of Arsenic Adsorption on Magnetite Nanoparticles from Water: Thermodynamic and Spectroscopic Studies. *Environ. Sci. Technol.* **2015**, *49*, 7726–7734.